

Sig-DEG for Distillation: Making Diffusion Models Faster and Lighter

Lei Jiang

University College London
lei.j@ucl.ac.uk

Wen Ge *

University College London
wen.ge@alumni.lse.ac.uk

Niels Cariou-Kotlarek

University College London
niels.kotlarek.23@ucl.ac.uk

Mingxuan Yi †

JPMorganChase
mingxuan.yi@jpmorgan.com

Po-Yu Chen †

JPMorganChase
po-yu.chen@jpmorgan.com

Lingyi Yang

University of Oxford
lingyi.yang@maths.ox.ac.uk

Francois Buet-Golfouse†

AIML Global Markets, Barclays
francois.buetgolfouse@barclays.com

Gaurav Mittal†

AIML Global Markets, Barclays
gaurav.mittal1@barclays.com

Hao Ni

University College London
h.ni@ucl.ac.uk

Abstract

Diffusion models have achieved state-of-the-art results in generative modelling but remain computationally intensive at inference time, often requiring thousands of discretization steps. To this end, we propose Sig-DEG (Signature-based Differential Equation Generator), a novel generator for distilling pre-trained diffusion models, which can universally approximate the backward diffusion process at a coarse temporal resolution. Inspired by high-order approximations of stochastic differential equations (SDEs), Sig-DEG leverages partial signatures to efficiently summarize Brownian motion over sub-intervals and adopts a recurrent structure to enable accurate global approximation of the SDE solution. Distillation is formulated as a supervised learning task, where Sig-DEG is trained to match the outputs of a fine-resolution diffusion model on a coarse time grid. During inference, Sig-DEG enables fast generation, as the partial signature terms can be simulated exactly without requiring fine-grained Brownian paths. Experiments demonstrate that Sig-DEG achieves competitive generation quality while reducing the number of inference steps by an order of magnitude. Our results highlight the effectiveness of signature-based approximations for efficient generative modeling.

*This author is expected to start her study at UCL in September 2025.

†**Disclaimer** - The authors' views are their own. The authors' employers past and present make no representation and warranty whatsoever and disclaim all liability, for the completeness, accuracy or reliability of the information contained herein. This document is not intended as investment research or investment advice, or a recommendation, offer or solicitation for the purchase or sale of any security, financial instrument, financial product or service, or to be used in any way for evaluating the merits of participating in any transaction, and shall not constitute a solicitation under any jurisdiction or to any person, if such solicitation under such jurisdiction or to such person would be unlawful.

1 Introduction

Diffusion models [Sohl-Dickstein et al., 2015, Ho et al., 2020, Song et al., 2021] have become a cornerstone of modern generative modelling, achieving state-of-the-art performance in high-fidelity image synthesis and beyond [Dhariwal and Nichol, 2021]. These models define a generative process by reversing a stochastic differential equation (SDE) that gradually transforms data into noise. By learning to approximate the time-reversal of this process, diffusion models can sample from complex data distributions by iteratively denoising from a noise prior.

However, the generation process in diffusion models remains computationally expensive, often requiring hundreds or thousands of fine-grained steps to discretize the reverse SDE. This creates a significant bottleneck for real-time or resource-constrained applications. A growing body of work seeks to accelerate inference by distilling high-quality, pre-trained diffusion models into compact surrogates that retain generation fidelity (e.g., consistency model [Song et al., 2023] and phase consistency model [Kim et al., 2023]). Yet most existing approaches rely on architectural heuristics or ignore the underlying SDE structure altogether.

In this work, we propose a principled alternative: Signature-based Differential Equation Generator (**Sig-DEG**), a fast and lightweight surrogate for pre-trained diffusion models that directly approximates the reverse-time SDE using tools from stochastic analysis and rough path theory. Our method builds on the observation that high-order numerical schemes – particularly those based on stochastic Taylor expansions – allow for accurate approximation of SDE solutions using coarse discretizations. Specifically, we introduce the use of *partial signatures*, a low-dimensional and tractable subset of path signatures [Lyons et al., 2007], to efficiently summarize the Brownian motion trajectories over each sub-time interval and enable accurate global approximation of the SDE solution. The partial signature acts as a principled feature extractor for Brownian motion, whose dimension is independent of the underlying discretization resolution. Compared with directly using discretized Brownian motion, this representation substantially reduces dimensionality while preserving essential information of SDE approximation, thereby improving both accuracy and robustness.

Sig-DEG models the generative process as a discrete-time recurrence over coarse time steps. At each step, a recurrent neural network consumes the current latent state and the analytically simulable partial signature to produce the next point in the reverse trajectory. Training is performed via supervised distillation from a high-resolution teacher model using a simple mean squared error objective. Crucially, because the distribution of partial signatures is known in closed form, Sig-DEG avoids the need to reconstruct fine-resolution Brownian paths at inference time – leading to orders-of-magnitude acceleration while maintaining high generative quality. The overall workflow of training Sig-DEG for distilling the diffusion model is given in Figure 1.

Unlike consistency-based distillation methods, which enforce trajectory coherence through specialized losses or architectural constraints, Sig-DEG naturally respects the underlying SDE structure. Its design is grounded in approximation theory, offering both theoretical guarantees and empirical efficiency.

Contributions. Our work introduces Sig-DEG, a novel SDE-based distillation framework, with the following key contributions:

1. We reformulate distillation as a supervised learning task, learning the mapping between the driving noise trajectory and the reverse diffusion process on a coarse time grid.
2. We propose the Sig-DEG model, which is theoretically grounded in high-order stochastic Taylor expansions and leverages the closed-form distribution of partial signatures for exact simulation and fast inference.
3. We demonstrate strong performance across diverse modalities – including images and rough volatility time series – achieving 50–100× faster inference with competitive generation quality.

1.1 Related Work

1.1.1 Consistency-based Distillation Models

Consistency models (CMs) [Song et al., 2023] aim to bypass the slow, stepwise sampling in diffusion models by learning a direct map from noisy inputs to clean data, enforcing consistency across different

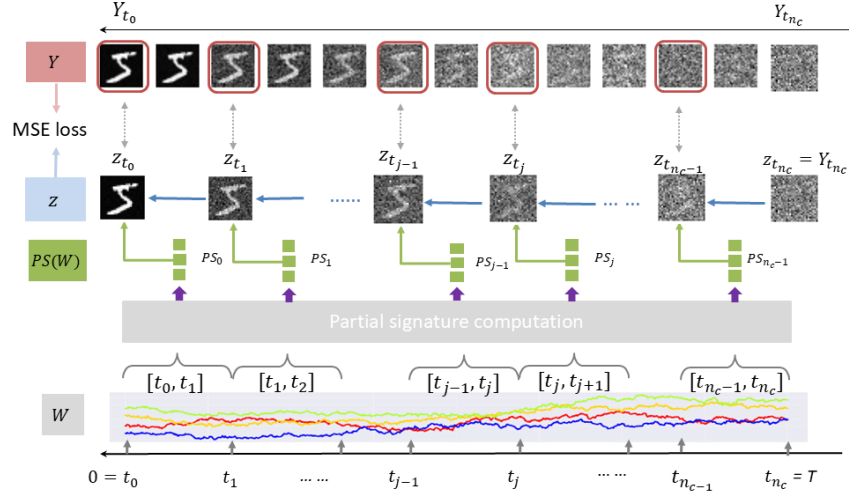


Figure 1: **Overview of Sig-DEG for distilling diffusion models.** A teacher diffusion model generates fine-resolution reverse trajectories driven by Brownian noise. Instead of reconstructing these full trajectories, Sig-DEG leverages analytically tractable partial signatures to summarize the noise over coarse intervals. A generator then consumes the noisy latent state and partial signatures to produce the next step in the backward process. Training is performed via supervised distillation with a mean squared error loss, ensuring that Sig-DEG learns to approximate the teacher model on a coarse time grid. This design allows Sig-DEG to achieve orders-of-magnitude acceleration in sampling while preserving the theoretical structure of the underlying SDE.

noise levels. This enables fast sampling – often in a single step – while retaining optional refinement via multiple evaluations.

Consistency Trajectory Models (CTMs) [Kim et al., 2023] generalize this approach to multistep sampling by training networks that remain consistent along entire noise trajectories. More recently, Phased Consistency Models (PCMs) [Wang et al., 2024] focus training on the boundary points actually used at inference time, reducing redundancy in intermediate supervision. Consistency models and their variants learn to approximate the solution operator of the Probability Flow ODE, mapping a noisy state X_t (from the forward process) directly back to a clean sample X_0 . This is in stark contrast to our setting, where the goal of our method is to learn the mapping between the noise trajectory and the backward process evaluated on a coarse time partition. Moreover, the architectures of CTMs and PCMs are based on ordinary differential equations (ODEs) and uses the skip connections, but they do not exploit the intrinsic structure of the underlying SDEs, which our method leverages.

1.1.2 Neural Differential Equation Models

Our work is related to the broader class of neural differential equation models, including neural ODEs [Chen et al., 2018], neural controlled differential equations (CDEs) [Kidger et al., 2020, Morrill et al., 2021a], and neural SDEs [Kidger et al., 2021]. These models represent data trajectories as solutions to parametrized continuous-time dynamics, enabling flexible modelling of temporal processes. Of particular relevance are neural SDEs, which model stochastic trajectories directly but typically rely on low-order solvers such as Euler-Maruyama, limiting their scalability for inference-intensive tasks like diffusion sampling.

Sig-DEG also connects to a line of work on neural approximations of controlled differential equations using path signatures – especially Logsig-RNNs [Liao et al., 2019, 2021] and Neural rough differential equations (RDEs) [Morrill et al., 2021b]. These architectures leverage signature features to model complex temporal dependencies, drawing from rough path theory. However, existing signature-based

models often require intractable simulations of high-order signature terms, particularly for stochastic drivers like Brownian motion.

In contrast, Sig-DEG leverages a carefully chosen subset of signature terms, which we call *partial signatures*, that are both analytically tractable and sufficient for high-order SDE approximation. This preserves theoretical fidelity while achieving fast, exact simulation and practical speed-ups.

2 Preliminaries

In this section, we introduce the preliminaries on the diffusion model for data generation and the high-order approximation of stochastic differential equations based on stochastic Taylor expansion.

2.1 Diffusion Model

Diffusion models are a class of generative models that learn to synthesize data by modeling the reversal of a stochastic noising process. The *forward process*, also known as the diffusion process, incrementally adds Gaussian noise to data over a fixed number of time steps T . More precisely

$$dX_t = f(X_t, t)dt + \sigma_t \cdot dW_t, \quad X_0 \sim p_{\text{data}}, \quad (1)$$

where $t \in [0, T]$, $f(X_t, t)$ and σ_t represent the drift and diffusion terms respectively, and \cdot represents the Itô integral where dW_t is the standard Wiener process.

Given the forward noising process to perturb data into noise, there exists an associated denoising process to reverse the forward noising process [Song et al., 2021], known as the *backward process*

$$dY_t = (f(Y_t, t) - \sigma_t^2 \nabla \log p(t, Y_t))dt + \sigma_t d\tilde{W}_t, \quad Y_T \sim p_{\text{noise}}, \quad (2)$$

where \tilde{W}_t is the reversed standard Wiener process, with time t evolving backwards, and $\log p(t, Y_t)$ is the score function of the marginal probability $p(t, \cdot)$. The score function can be modelled via a time-dependent neural net, $s_\theta(X_t, t)$, and training diffusion models can be achieved by minimizing the score matching objective

$$\mathbb{E}_{t \sim [0, T]} \mathbb{E}_{X_0 \sim p_{\text{data}}} \mathbb{E}_{X_t \sim p(X_t | X_0)} \left[\lambda(t) \|\nabla_{X_t} \log p(X_t | X_0) - s_\theta(X_t, t)\|_2^2 \right], \quad (3)$$

where $\lambda(t)$ is a weighting function.

2.2 High-Order Approximation of SDEs

It is well-known that there is a one-to-one, explicit correspondence between the Itô and Stratonovich integral (see Appendix A.1). Given that numerical approximation theory has a simpler representation for Stratonovich SDEs compared to Itô SDEs, we consider the general SDE in the Stratonovich sense as follows:

$$dY_t = \mu(t, Y_t)dt + \sigma_t \circ dW_t, \quad \forall t \in [0, T], \quad (4)$$

where \circ is the Stratonovich integral. In fact, in the diffusion model, as σ is a deterministic function w.r.t. t , the forward / backward process defined by Eqn. (1) / Eqn. (2) coincides with their Stratonovich SDEs. For simplicity, we assume that the vector fields μ and σ are smooth.

Stochastic Taylor Expansion. By Baudoin [2012], Kloeden et al. [1992], one has that for any $0 \leq s \leq t$ and $t - s$ is sufficiently small,

$$Y_t \approx Y_s + \mu(s, Y_s)(t - s) + \sigma_s(W_t - W_s) + \partial_y \mu(s, Y_s) \sigma_s \int_s^t \int_s^u dW_{s_1} du + \dots$$

It means that there exists $\varepsilon > 0$ and a function F such that for any $|t - s| \leq \varepsilon$, the solution Y_t can be approximated by

$$Y_t \approx Y_s + F(s, Y_s, PS(W)_{s,t}), \quad (5)$$

where $PS(W)_{s,t} := (t - s, W_t - W_s, \int_s^t \int_s^u dW_{s_1} du)$. The function $F : \mathbb{R}^+ \times E \times \mathbb{R}^+ \times E \times E \rightarrow E$ has the following form:

$$F(s, y, s_1, s_2, s_{12}) = \mu(s, y)s_1 + \sigma_s s_2 + \partial_t \sigma_s(s_1 s_2 - s_{21}) + \partial_y \mu(s, y) \sigma_s s_{21}.$$

The derivation of function F can be found in Appendix A.2. The features $PS(W)_{s,t}$ correspond to the informative subset of the signature (up to degree 2) of a time-augmented path W from s to t , and stands for *partial signature*. It is easy to see the recurrence of the partial signature, for any $0 \leq s \leq u \leq t$,

$$PS_{s,u} + PS_{u,t} = PS_{s,t} + (0, 0, W_{s,u}(t-u)), \quad PS_{s,s} = 0. \quad (6)$$

This simple recurrence enables the efficient computation of the partial signature of a piecewise linear approximation of Brownian motion, with linear-time complexity. See Appendix A for the formal definition of the path signature and a rigorous statement of the stochastic Taylor expansion.

Numerical Approximation Scheme. To approximate the terminal value Y_T effectively, we discretize the time interval $[0, T]$ into a finite partition $D_c = \{0 = t_0 < t_1 < \dots < t_{n_c} = T\}$ and let $\Delta t_c = \max_{i \in \{1, \dots, n_c\}}(t_i - t_{i-1})$ denote its time mesh. On each subinterval, we leverage the local approximation derived from the stochastic Taylor expansion, and construct a global approximation by iteratively composing these local solutions. More specifically, set $\hat{Y}_{t_0} = Y_0$. Then for $i \in \{0, \dots, n_c - 1\}$, set

$$\hat{Y}_{t_{i+1}} = \hat{Y}_{t_i} + F(t_i, Y_{t_i}, PS(W)_{t_i, t_{i+1}}). \quad (7)$$

Theorem 1. *Under standard regularity conditions on μ and σ , and assuming that σ only depends on t , then $\hat{Y}_{t_{n_c}}$ approximates Y_T in the strong sense with a local error of order $\mathcal{O}(\Delta t_c^2)$.*

Theorem 2. *Under standard regularity conditions on μ and σ , and assuming Brownian motion as the driving noise, the scheme in Eq. (7) yields a strong approximation of Y_T with a global error $\mathcal{O}(\Delta t_c)$.*

See Appendix A.2 for more details.

Remark 3. *This is in contrast to the Euler–Maruyama scheme, which achieves only $\mathcal{O}(\Delta t_c^{0.5})$ strong error. See Kloeden et al. [1992] for a comprehensive treatment of these results. The inclusion of second-order terms from the partial signature allows Sig-DEG to achieve high accuracy even on coarse time grids.*

Moreover, the joint distribution of $(PS(W)_{t_i, t_{i+1}})_i$ is explicitly known, as detailed in the following lemma and can be simulated exactly. The proof is deferred to Appendix A.4.

Lemma 4. *Given the time partition $D_c := \{t_i\}_{i=0}^{n_c}$, each $PS(W)_{t_{i-1}, t_i}$ is mutually independent across i . For $0 \leq s \leq t$, $(W_t - W_s, \int_s^t \int_s^u dW_{s_1} du)$ is a Gaussian random variable with mean zero and covariance matrix*

$$\Sigma = \begin{bmatrix} t-s & \frac{(t-s)^2}{2} \\ \frac{(t-s)^2}{2} & \frac{(t-s)^3}{3} \end{bmatrix}. \quad (8)$$

3 Sig-DEG Model for Diffusion Model Distillation

For efficient model distillation, we focus on fitting the backward process of the pre-trained diffusion model at a coarse time partition. To achieve this, we propose a signature-based differential equation generator (**Sig-DEG**) to approximate this backward process at the coarse resolution, reformulating the model fitting problem as a supervised learning task by using fine-resolution noise information, to enable faster inference without relying on fine-resolution noise during data generation.

Throughout this section, let $D_f = \{t_0, t_1, \dots, t_{N_f-1}\}$ and $D_c = \{s_0, s_1, \dots, s_{N_c-1}\}$ denote the fine-resolution partition and coarse-resolution partitions, with cardinalities $N_f > N_c$, respectively. We assume, without loss of generality, that the time partitions are equally spaced and that $D_c \subset D_f$. Let W denote the d -dimensional Brownian motion defined on $[0, T]$.

3.1 Sig-DEG Model

Motivated by the high-order numerical approximation scheme of SDEs in Section 2.2, we propose the generator of Sig-DEG, which parameterizes the vector field in Eqn. (7) by neural networks.

Definition 5 (Sig-DEG backward model). *Let $q \in \mathbb{N}$ and W denote Brownian motion. A q -step Sig-DEG, or in short q -Sig-DEG, denoted by $G_\theta^q(\cdot; W) : \mathcal{P}(\mathbb{R}^d) \times D_c \rightarrow \mathcal{P}(\mathbb{R}^{d \times q}) : (Z_q, t = t_j) \mapsto (Z_{q-1}, \dots, Z_0)$, where (Z_{q-1}, \dots, Z_0) is defined recursively by*

$$Z_{i-1} = Z_i + N_\theta(Z_i, t_{j-i}, PS(W)_{t_i, t_{i-1}}), \quad (9)$$

for each $i \in \{1, \dots, q\}$, where $N_\theta : \mathbb{R}^d \times \mathbb{R}^+ \times \mathbb{R}^d \rightarrow \mathbb{R}^d$ is a neural network, fully parametrized by θ . Here Z_i and $PS(W)_{t_i, t_{i-1}}$ are independent.

In the Sig-DEG backward generator, Z_q serves as the terminal condition and $t = t_j$ denotes the current time. By applying Eqn. (9) recursively, the Sig-DEG produces the first q -step time series at time t_{j-1}, \dots, t_{j-q} backwards.

Sig-DEG enjoys the universality property, allowing it to approximate solutions of a broad class of SDEs, including those underlying pre-trained diffusion models. It thus serves as a principled and effective model for approximating the backward process on a coarse time grid D_c . More precisely, when we set $q = N_c$ and $Z_q \sim p_{\text{noise}}$, the resulting Sig-DEG outputs the time series of length N_c , and enjoys the following universality.

Theorem 6 (Universality of Sig-DEG, informal). *Suppose that Y denotes the solution to the backward SDE of Eqn. (4) with the vector field (μ, σ) and the terminal condition $Y_T \sim p_{\text{noise}}$. Assume that (μ, σ, Y_T) satisfies some regularity conditions. Fix any compact set $K \subset S(V_p([0, T], \mathbb{R}^d))$. For every $\varepsilon > 0$, there exists sufficiently small $\Delta t_c > 0$, such that*

$$\sup_{W \in K} \|G_\theta^{N_c}(Y_T, T; W) - Y_0\| \leq \varepsilon.$$

A more precise statement and proof can be found in Appendix B.

3.2 Supervised Learning Module

Given the pre-trained diffusion model g_ϕ , we construct the dataset comprising input-output pairs (W_{D_f}, Y_{D_c}) where W_{D_f} is the discretized Brownian motion sampled at D_f , and Y_{D_c} denotes the backward process downsampled at $t \in D_c$, which is generated by g_ϕ and driven by the Brownian path W . Our objective is to train the Sig-DEG model to learn the functional relationship between these input-output pairs. When the sample-wise loss in the supervised learning module is small, it implies that the Sig-DEG's output at $t_0 = 0$ closely approximates the distribution of $Y_0 \approx p_{\text{data}}$.

Recall that Sig-DEG's output is denoted by $G_\theta^{n_c}(Y_T, T; W_{D_f})$, which aims to approximate the backward process evaluated at D_c . The global learning objective is given by

$$\mathcal{L}_\theta := \mathbb{E}_{p \sim g_\phi} [\|Y_{D_c} - G_\theta^{n_c}(Y_T, T; W_{D_f})\|^2], \quad (10)$$

where $\|\cdot\|$ is the l_2 norm and the expectation is taken over the joint distribution (W, Y) , induced by the pretrained diffusion model g_ϕ (denoted by $\mathbb{E}_{p \sim g_\phi}$).

Local loss for training acceleration. Computing the global loss \mathcal{L}_θ (Eqn. (10)) over the entire coarse time partition D_c can be computationally intensive. To accelerate the training process, we introduce a local learning objective by uniformly sampling a time point $t \in D_c$ and matching the next q coarse steps per iteration for a small q . More specifically, we uniformly sample $j \in \{q, \dots, n_c\}$ and let $t = t_j$, the local loss is defined by

$$\mathcal{L}_\theta^{\text{local}}(t_j) := \mathbb{E}_{p \sim g_\phi} [\|Y_{t_{j-q}:t_{j-1}} - G_\theta^q(Y_{t_j}, t_j, W)\|^2]. \quad (11)$$

The expected value of the local loss (over the uniform distribution on time t) is given by

$$\mathbb{E}_{t \sim \mathcal{U}(D_c)} [\mathcal{L}_\theta^{\text{local}}(t)] \approx \mathcal{L}_\theta. \quad (12)$$

We present the pseudo-code in Algorithm 1 to clearly detail the training process. The coarse step q is set to 1 by default in the pseudo-code for simplicity.

3.3 Inference with Exact Simulation

Once the Sig-DEG model is trained, inference is performed by simulating the estimated backward process over a coarse time partition. More specifically, we start with generating $Z_{N_c} \sim p_{\text{noise}}$. Then for each $i \in \{N_c - 1, \dots, 1\}$, we directly simulate $PS(W_{t_i, t_{i+1}})$ using Lemma 4, and apply the recurrence Eqn. (9) to compute $Z_{t_{i-1}}$ from Z_{t_i} , ultimately yielding $Z_0 \approx p_{\text{data}}$. Importantly, note that the simulation of $PS(W_{t_i, t_{i+1}})$ is exact and does not require simulating the Brownian motion at fine resolution. As a result, it avoids any time discretization error and the Sig-DEG's inference time is independent of the fine time resolution, scaling linearly with the coarse time dimension N_c . Since the time dimension of Sig-DEG, N_c , is typically much smaller than that of the pre-trained diffusion model, N_f , the proposed model results in significant acceleration of inference time while maintaining high-quality generation.

Algorithm 1 Sig-DEG Supervised Learning Training

```
1: Initialize: Teacher model  $g_\phi = (\mu, \sigma, f_\phi)$ , with  $\mu$  and  $\sigma$  being the drift and diffusion coefficient
   of the forward process with the perturbation kernel  $p(X_t|X_0)$  determined by  $\mu$  and  $\sigma$ , and  $f_\phi$ 
   (the score net),  $G_\theta$  the Sig-DEG Generator, and  $\eta > 0$  the learning rate.  $D_c = (t_i)_{i=1}^{N_c}$  – coarse
   time partition.  $D_f = (s_j)_{j=1}^{N_c \cdot r}$  – fine time partition, where  $r \in \mathbb{N}$ .
2: repeat
3:    $x_0 \sim p_{\text{data}}, j \sim \mathcal{U}(\{1, \dots, N_c\}), \varepsilon \sim \mathcal{N}(0, \mathbf{I})$ .
4:    $s \leftarrow t_{j-1}$  and  $t \leftarrow t_j$ .
5:   Generate  $Y_t$  using  $Y_t = \mu(t)X_0 + \sigma_t \varepsilon$ . ▷ Forward SDE:  $Y_t \sim p(Y_t|X_0 = x_0)$ 
6:    $\mathcal{W} \leftarrow \mathbf{0} \in \mathbb{R}^{2d+1}$ 
7:   for  $l \in [j \cdot r : (j-1) \cdot r]$  do
8:     Sample noise:  $\zeta_l \sim \mathcal{N}(0, \mathbf{I})$ 
9:     Construct the Brownian motion increment:  $W_{s_{l-1}, s_l} \leftarrow \zeta_l \cdot \sqrt{\Delta_f}$ , where  $\Delta_f = \frac{1}{N_c \cdot r}$ .
10:    Update  $Y_{s_{l-1}} \leftarrow g_\phi(Y_{s_l}, W_{s_l, s_{l-1}})$ 
11:    Update PS term:  $\text{PS}(\mathcal{W})_{s,t} \leftarrow \text{PS}(\mathcal{W})_{s,t} + (W_{s_l, s_{l-1}}, s_l - s_{l-1}, W_{s, s_l}(s_l - s_{l-1}))$  ▷
    Compute the PS of  $W$  by the recurrence shown in Eqn. 6.
12:   end for
13:   Generate prediction:  $\hat{Y}_s \leftarrow Y_t + G_\theta(Y_t, t, \text{PS}(\mathcal{W})_{s,t})$ 
14:   Compute loss:  $\mathcal{L}(\theta) \leftarrow \text{MSE}(\hat{Y}_{t_{l-1}}, Y_{t_{l-1}})$ 
15:   Update Sig-DEG generator:  $\theta \leftarrow \theta - \eta \nabla_\theta \mathcal{L}(\theta)$ .
16: until convergence
```

4 Numerical Experiments

To evaluate the performance and generalizability of the proposed Sig-DEG model, we perform experiments on datasets that span synthetic distributions, images, and financial time series. Specifically, we evaluate the model on the following benchmarks of various modalities: (1) one-dimensional Gaussian mixture distributions (**1DN**), (2) image dataset of handwritten digits (**MNIST**), and (3) rough volatility time series (**rBerg**).

For each dataset, we compare the generative performance of Sig-DEG with the baseline diffusion models used for training the distilled model. All experimental configurations, including dataset specifications, hyperparameter settings, and detailed metric definitions, are documented in Appendix C. Unless otherwise specified, Sig-DEG refers to the 1-step Sig-DEG model, with $q = 1$.

4.1 Few-Step Data Generation

4.1.1 One-Dimensional Gaussian Mixture Experiment

To evaluate the effectiveness of the proposed methodology, we perform an experiment on a synthetic one-dimensional Gaussian mixture dataset **1DN**. Figure 2 illustrates the backward trajectories generated by the proposed Sig-DEG method compared with those of the teacher model. Using only 5 sampling steps, Sig-DEG closely reproduces the 300-step teacher trajectories, achieving a $7\times$ reduction in inference time without compromising sample quality (see Table 1). These findings suggest that Sig-DEG provides a computationally efficient alternative to conventional sampling techniques without sacrificing sample fidelity.

4.1.2 Handwritten Digit Generation on MNIST

We next evaluate Sig-DEG on **MNIST**, a canonical high-dimensional benchmark comprising grayscale images of handwritten digits. Table 2 presents results comparing Sig-DEG and the teacher model at 1000 and 1500 diffusion steps. Sig-DEG reduces inference time by over $40\times$, while preserving or improving sample quality, as measured by Fréchet inception distance (FID) and Inception Score (IS). With only 10 sampling steps, Sig-DEG achieves an FID of 4.92 and IS of 9.40, outperforming the 1500-step teacher model in both metrics (Table 2).

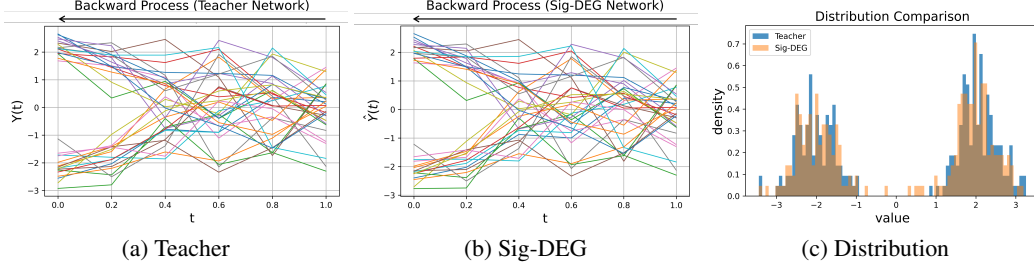


Figure 2: **Few-step generation results on the 1D Gaussian mixture.** (a) 300-step teacher trajectories. The black arrow indicates the direction of the backward process. (b) Sig-DEG with 5 steps. (c) Comparison of final sample distributions. Histograms of the marginal distributions show minimal discrepancy between the models.

4.1.3 Time Series Generation on Rough Volatility Data

We next turn to time series generation under rough stochastic volatility, a substantially more challenging domain due to irregularity and latent dependence structures. **RBerg** consists of two interdependent components: the log-price and log-volatility series. These processes are characterized by low Hölder regularity and intricate cross-dependencies, making it essential to evaluate generated samples not only via distributional losses (e.g., marginal distribution loss and Wasserstein-1), but also through correlation and autocorrelation metrics that assess temporal fidelity. At 10 sampling steps, Sig-DEG achieves a marginal distribution loss of 0.0680 ± 0.0005 and a Wasserstein-1 distance of 0.0249 ± 0.0052 , while recovering temporal structure with lower correlation (0.0172 ± 0.00014) and autocorrelation (0.0054 ± 0.00030) errors than the teacher model. This yields a 24-fold reduction in inference time (Table 3). Even with a single sampling step, Sig-DEG retains reasonable distributional fidelity, achieving a $267\times$ speed-up with moderate increases in approximation error (Table 3).

Figures in Appendix C.4.4 compare the outputs of the teacher model with those of Sig-DEG under a 10-step configuration. The analysis includes both trajectory evolution and the marginal distributions of log-increments. The Sig-DEG trajectories exhibit high fidelity to the reference dynamics, while the marginal distributions’ histograms display only minimal deviations, validating the model’s capacity to replicate complex stochastic features inherent in rough volatility time series.

Table 1: Performance and speed-up comparison on **1DN**.

Method	Wasserstein ↓	Variance ↓	Time (min)	× Speed
Teacher (300)	0.56 ± 0.30	0.51 ± 0.38	0.42	—
Sig-DEG (10)	0.64 ± 0.35	0.58 ± 0.36	0.07	6
Sig-DEG (5)	0.57 ± 0.26	0.62 ± 0.50	0.06	7

Table 2: Comparison of performance on the **MNIST** dataset using 1000 and 1500 sampling steps. Inference times correspond to the complete test set with a batch size of 128.

Method	1000 steps				1500 steps			
	FID ↓	IS ↑	Time (min)	× Speed	FID ↓	IS ↑	Time (min)	× Speed
Teacher (Var.)	6.70	9.11 ± 0.07	16.16	—	5.61	9.30 ± 0.08	33.23	—
Sig-DEG (10)	6.11	9.16 ± 0.05	0.41	39	4.92	9.40 ± 0.05	0.40	83
Sig-DEG (5)	6.64	9.17 ± 0.09	0.32	51	5.12	9.39 ± 0.08	0.33	101
Sig-DEG (1)	10.70	8.96 ± 0.07	0.26	62	8.32	9.29 ± 0.06	0.26	128

4.2 Model Complexity Analysis

We first evaluate the impact of generator parameter count on **MNIST** performance (see Tables 4 and 5). We distill the generator of our sig-DEG (5 sampling steps) from a 1,500-step diffusion teacher. We vary network depth and feature dimensionality. Architecture details are given in Appendix C.

Table 3: **rBerg** dataset. Sig-DEG vs. baseline comparison on marginal distribution histogram loss, Wasserstein-1 distance, correlation, and inference speed (mean \pm standard deviation over 10 runs) for a batch of 20k samples.

Method	Marg. Dist. \downarrow	W-1 \downarrow	Corr \downarrow	AutoCorr \downarrow	Time (min)	\times Speed
Teacher (1K steps)	0.0597 \pm 4.4e-4	0.0210 \pm 1.1e-3	0.0360 \pm 6.9e-3	0.0139 \pm 2.6e-3	9.93 $\times 10^{-2}$ \pm 9.10 $\times 10^{-4}$	–
Sig-DEG (10 steps)	0.0680 \pm 5.0e-4	0.0249 \pm 5.2e-3	0.0172 \pm 1.4e-4	0.0054 \pm 3.0e-4	4.17 $\times 10^{-3}$ \pm 1.95 $\times 10^{-5}$	24
Sig-DEG (5 steps)	0.0673 \pm 4.1e-4	0.0321 \pm 6.6e-4	0.0171 \pm 2.5e-4	0.0060 \pm 1.5e-4	2.12 $\times 10^{-3}$ \pm 1.78 $\times 10^{-5}$	48
Sig-DEG (1 step)	0.0923 \pm 3.5e-4	0.0643 \pm 2.6e-4	0.0177 \pm 2.1e-4	0.0078 \pm 2.5e-4	3.72 $\times 10^{-4}$ \pm 1.82 $\times 10^{-5}$	267

Table 4: **MNIST** dataset feature dimension ratio.

Method	# Params	FID	IS	Time (min)
Full	19.855	5.12	9.39 \pm 7.8e-2	0.33
3/4	11.514	4.93	9.31 \pm 7.6e-2	0.33
1/2	4.980	4.98	9.35 \pm 7.4e-2	0.32
[1/4, 1/2]	2.890	5.72	9.37 \pm 4.0e-2	0.33
1/4	1.253	5.56	9.27 \pm 7.9e-2	0.33

Table 5: **MNIST** dataset block number variation.

Method	# Params	FID	IS	Time (min)
Full	19.855	5.12	9.39 \pm 7.8e-2	0.33
11 blocks	15.126	4.86	9.32 \pm 9.5e-2	0.32
10 blocks	13.550	5.97	9.20 \pm 6.1e-2	0.32
8 blocks	12.727	5.38	9.27 \pm 6.9e-2	0.31
7 blocks	11.150	5.05	9.35 \pm 5.1e-2	0.29

The results suggest that the generator is robust to moderate reductions in model size. From Table 4 and 5, we see that halving the dimensionality of the feature reduces the parameters by 75% (19.9 M to 5.0 M) with only a 1% FID increase (4.93 to 4.98) and stable IS (9.31 to 9.35). Interestingly, the half-dimension variant achieves the best FID (4.86), indicating that moderate compression can improve sample fidelity. Compressing both depth and width to yield 2.8 M parameters results in only a slight increase in FID and negligible change in IS, underscoring the robustness to aggressive pruning. These findings highlight the efficiency and scalability of the distilled generator design.

Overall, both **MNIST** and **rBerg** experiments demonstrate that Sig-DEG can be compressed by up to 75% with minimal performance loss (Tables 4, 5, and 6), enabling further inference-time reductions.

4.3 Effect of q on Sig-DEG

We evaluate how the number of steps q , influences the performance of our Sig-DEG student models. For the **MNIST** dataset, we analyse models distilled from a 1500-step teacher model (Table 7). For a 5-step generation budget, the lowest FID (5.12) is achieved at $q = 1$, with FID rising marginally to 5.20 and 5.23 for $q = 2$ and $q = 4$, respectively, while the Inception Score remains constant at ≈ 9.39 . In the 10-step case, $q = 2$ yields the best FID, 4.74 versus 4.92 at $q = 1$ and 5.28 at $q = 4$, again with IS largely unaffected (≈ 9.37). Similar trends are observed on the **rBerg** dataset. Note that $q > 1$ comes at the cost of increased training time. Hence we fix $q = 1$ in all of our experiments to balance performance and training efficiency.

5 Conclusion & Broader Impact

Conclusion. We introduced **Sig-DEG**, a principled distillation framework that accelerates sampling in diffusion models by orders of magnitude via partial path signatures and a recurrent approximation of the reverse-time SDE. Grounded in stochastic Taylor expansions and rough path theory, Sig-DEG achieves **5–10 step** generative inference with **50–100 \times speedups** – all while maintaining or improving fidelity on image and time series benchmarks. Crucially, the architecture is modular, lightweight, and model-agnostic, opening the door to broader applicability beyond traditional diffusion solvers.

This work bridges numerical SDE approximation and generative modeling, offering one of the first end-to-end frameworks that integrates rough path theory into modern neural distillation. Sig-DEG sidesteps handcrafted schedulers or implicit solvers by leveraging exact simulation of signature features, yielding a distillation approach that is both mathematically grounded and empirically effective.

Table 6: **rBerg** dataset: Comparison of model complexity and performance across network configurations (mean \pm standard deviation over 10 runs). Inference time corresponds to generating 20k samples.

# Blocks	Block Size	# Params [10 ⁶]	Marg. Dist. Loss \downarrow	W-1 \downarrow	Corr \downarrow	AutoCorr \downarrow	Time (min)
3	256	0.808	0.0725 \pm 5.0e-4	0.0304 \pm 6.0e-4	0.0172 \pm 5.0e-4	0.0055 \pm 3.0e-4	2.22 \times 10 ⁻³ \pm 1.64 \times 10 ⁻⁴
2	256	0.611	0.0727 \pm 3.0e-4	0.0296 \pm 8.0e-4	0.0171 \pm 2.0e-4	0.0058 \pm 2.0e-4	2.27 \times 10 ⁻³ \pm 3.69 \times 10 ⁻⁴
1	256	0.413	0.0713 \pm 3.0e-4	0.0329 \pm 6.0e-4	0.0169 \pm 3.0e-4	0.0060 \pm 3.0e-4	2.19 \times 10 ⁻³ \pm 2.62 \times 10 ⁻⁴
2	128	0.174	0.1113 \pm 4.0e-4	0.0699 \pm 7.0e-4	0.0163 \pm 2.0e-4	0.0063 \pm 4.0e-4	2.09 \times 10 ⁻³ \pm 2.92 \times 10 ⁻⁴
1	128	0.125	0.1038 \pm 6.0e-4	0.0670 \pm 4.0e-4	0.0163 \pm 2.0e-4	0.0058 \pm 3.0e-4	1.93 \times 10 ⁻³ \pm 1.85 \times 10 ⁻⁴
3	192	0.471	0.0753 \pm 6.0e-4	0.0351 \pm 8.0e-4	0.0171 \pm 4.0e-4	0.0060 \pm 5.0e-4	2.15 \times 10 ⁻³ \pm 2.46 \times 10 ⁻⁴
3	128	0.224	0.1201 \pm 5.0e-4	0.0733 \pm 7.0e-4	0.0214 \pm 5.0e-4	0.0072 \pm 3.0e-4	2.10 \times 10 ⁻³ \pm 2.93 \times 10 ⁻⁴
3	64	0.670	0.1725 \pm 3.0e-4	0.1164 \pm 3.0e-4	0.0262 \pm 1.0e-4	0.0108 \pm 3.0e-4	2.07 \times 10 ⁻³ \pm 2.50 \times 10 ⁻⁴
3	32	0.220	0.1726 \pm 5.0e-4	0.1109 \pm 3.0e-4	0.0471 \pm 2.0e-4	0.0178 \pm 2.0e-4	2.05 \times 10 ⁻³ \pm 2.65 \times 10 ⁻⁴

Table 7: Comparison of Sig-DEG performance on **MNIST** and **rBerg** across q -step configurations. Effect of varying the q -step on the performance of the Sig-DEG generator. Results are shown for distilled models with 5 and 10 total sampling steps.

Steps	q	MNIST		rBerg			
		FID \downarrow	IS \uparrow	Marg. Dist. \downarrow	W-1 \downarrow	Corr \downarrow	AutoCorr \downarrow
5	1	5.12	9.39 \pm 7.8e-2	0.0659 \pm 5.7e-4	0.0279 \pm 5.6e-4	0.0172 \pm 2.4e-4	0.00584 \pm 2.6e-4
5	2	5.20	9.39 \pm 6.5e-2	0.0721 \pm 4.5e-4	0.0217 \pm 5.2e-4	0.0214 \pm 1.4e-4	0.00614 \pm 6.6e-4
5	4	5.23	9.39 \pm 7.5e-2	0.1202 \pm 3.8e-4	0.0734 \pm 3.9e-4	0.0186 \pm 2.6e-2	0.00647 \pm 4.4e-3
10	1	4.92	9.40 \pm 5.4e-2	0.0650 \pm 4.0e-4	0.0240 \pm 3.9e-4	0.0170 \pm 2.8e-4	0.0060 \pm 3.6e-4
10	2	4.74	9.36 \pm 6.4e-2	0.0638 \pm 4.0e-4	0.0177 \pm 4.0e-4	0.0171 \pm 2.8e-4	0.0051 \pm 3.7e-4
10	4	5.28	9.37 \pm 6.2e-2	0.0762 \pm 4.0e-4	0.0242 \pm 5.9e-3	0.0176 \pm 3.0e-2	0.0053 \pm 4.3e-3

Limitations & Future Work. In future work, we would like to apply Sig-DEG on more challenging and complex tasks, such as high-resolution image generation and conditional image generation based on textual description (e.g., Stable Diffusion). Additionally, while we use fixed-order partial signatures, a promising direction is to learn which features of the signature are most informative – adapting the truncation, selection, or weighting of PS terms during training. Finally, incorporating higher-order stochastic features (e.g., Lévy area) may further improve performance, and recent advances in cubature on Wiener space [Foster, 2020] and generative modeling of path functionals [Jelinčič et al., 2023] offer tractable ways forward.

Broader Impact. By significantly reducing the computational burden of diffusion-based generation, Sig-DEG enables resource-efficient deployment on edge devices (e.g. mobile phones and wearables) and contributes to more sustainable AI. At the same time, improving generative accessibility raises risks of misuse. We advocate for responsible integration with content watermarking, usage monitoring, and adversarial detection frameworks to mitigate potential harms.

Acknowledgments and Disclosure of Funding

HN, LJ, and LY are supported by the EPSRC [grant number EP/S026347/1]. HN is also supported by The Alan Turing Institute under the EPSRC grant EP/N510129/1. LY is also supported by the Hong Kong Innovation and Technology Commission (InnoHK Project CIMDA). NCK is supported by the Engineering and Physical Sciences Research Council [grant numbers EP/T517793/1, EP/W524335/1]. All authors thank the anonymous reviewers for their constructive comments that helped improve the manuscript.

References

- Fabrice Baudoin. Stochastic taylor expansions and heat kernel asymptotics. *ESAIM: Probability and Statistics*, 16:453–478, 2012.
- Christian Bayer, Peter Friz, and Jim Gatheral. Pricing under rough volatility. *Quantitative Finance*, 16(6):887–904, 2016.
- Mikkel Bennedsen, Asger Lunde, and Mikko S Pakkanen. Hybrid scheme for brownian semistationary processes. *Finance and Stochastics*, 21:931–965, 2017.
- Ricky TQ Chen, Yulia Rubanova, Jesse Bettencourt, and David K Duvenaud. Neural ordinary differential equations. *Advances in neural information processing systems*, 31, 2018.
- Prafulla Dhariwal and Alexander Nichol. Diffusion models beat gans on image synthesis. *Advances in neural information processing systems*, 34:8780–8794, 2021.
- Rémi Flamary, Nicolas Courty, Alexandre Gramfort, Mokhtar Z. Alaya, Aurélie Boisbunon, Stanislas Chambon, Laetitia Chapel, Adrien Corenflos, Kilian Fatras, Nemo Fournier, Léo Gautheron, Nathalie T.H. Gayraud, Hicham Janati, Alain Rakotomamonjy, Ievgen Redko, Antoine Rolet, Antony Schutz, Vivien Seguy, Danica J. Sutherland, Romain Tavenard, Alexander Tong, and Titouan Vayer. Pot: Python optimal transport. *Journal of Machine Learning Research*, 22(78): 1–8, 2021. URL <http://jmlr.org/papers/v22/20-451.html>.
- James Foster. *Numerical approximations for stochastic differential equations*. PhD thesis, University of Oxford, 2020.
- Peter K. Friz and Nicolas B. Victoir. *Multidimensional Stochastic Processes as Rough Paths*. Cambridge University Press, 2010. doi: 10.1017/CBO9780511845079.
- Jonathan Ho, Ajay Jain, and Pieter Abbeel. Denoising diffusion probabilistic models. In *Advances in Neural Information Processing Systems*, pages 6840–6851, 2020.
- Andraž Jelinčič, Jiajie Tao, William F Turner, Thomas Cass, James Foster, and Hao Ni. Generative modelling of lé vy area for high order SDE simulation. *arXiv preprint arXiv:2308.02452*, 2023.
- Patrick Kidger, James Morrill, James Foster, and Terry Lyons. Neural controlled differential equations for irregular time series. *Advances in neural information processing systems*, 33: 6696–6707, 2020.
- Patrick Kidger, James Foster, Xuechen Li, and Terry J Lyons. Neural sdes as infinite-dimensional gans. In *International conference on machine learning*, pages 5453–5463. PMLR, 2021.
- Dongjun Kim, Chieh-Hsin Lai, Wei-Hsiang Liao, Naoki Murata, Yuhta Takida, Toshimitsu Uesaka, Yutong He, Yuki Mitsufuji, and Stefano Ermon. Consistency trajectory models: Learning probability flow ODE trajectory of diffusion. *arXiv preprint arXiv:2310.02279*, 2023.
- Diederik P. Kingma and Jimmy Ba. Adam: A method for stochastic optimization. In Yoshua Bengio and Yann LeCun, editors, *ICLR (Poster)*, 2015. URL <http://dblp.uni-trier.de/db/conf/iclr/iclr2015.html#KingmaB14>.
- Peter E Kloeden, Eckhard Platen, Peter E Kloeden, and Eckhard Platen. *Stochastic differential equations*. Springer, 1992.
- Yann LeCun, Léon Bottou, Yoshua Bengio, and Patrick Haffner. Gradient-based learning applied to document recognition. *Proceedings of the IEEE*, 86(11):2278–2324, 1998.
- Daniel Levin, Terry Lyons, and Hao Ni. Learning from the past, predicting the statistics for the future, learning an evolving system. *arXiv preprint arXiv:1309.0260*, 2013.
- Shujian Liao, Terry Lyons, Weixin Yang, and Hao Ni. Learning stochastic differential equations using rnn with log signature features. *arXiv preprint arXiv:1908.08286*, 2019.
- Shujian Liao, Terry Lyons, Weixin Yang, Kevin Schlegel, and Hao Ni. Logsig-rnn: A novel network for robust and efficient skeleton-based action recognition. *The British Machine Vision Conference (BMVC)*, 2021.

- T Lyons and A McLeod. Signature methods in machine learning. *EMS Surveys in Mathematical Sciences*, 2025.
- Terry Lyons. Rough paths, signatures and the modelling of functions on streams. *Proceedings of the International Congress of Mathematicians*, 2014.
- Terry Lyons and Nicolas Victoir. Cubature on wiener space. *Proceedings of the Royal Society of London. Series A: Mathematical, Physical and Engineering Sciences*, 460(2041):169–198, 2004.
- Terry Lyons, Michael Caruana, and Thierry Lévy. *Differential Equations Driven by Rough Paths*, volume 1908 of *Lecture Notes in Mathematics*. Springer, 2007.
- Grigori Noikhovich Milstein. *Numerical integration of stochastic differential equations*, volume 313. Springer Science & Business Media, 2013.
- James Morrill, Patrick Kidger, Lingyi Yang, and Terry Lyons. Neural controlled differential equations for online prediction tasks. *arXiv preprint arXiv:2106.11028*, 2021a.
- James Morrill, Cristopher Salvi, Patrick Kidger, and James Foster. Neural rough differential equations for long time series. In *International Conference on Machine Learning*, pages 7829–7838. PMLR, 2021b.
- Robin Rombach, Andreas Blattmann, Dominik Lorenz, Patrick Esser, and Björn Ommer. High-resolution image synthesis with latent diffusion models. In *Proceedings of the IEEE/CVF conference on computer vision and pattern recognition*, pages 10684–10695, 2022.
- Jascha Sohl-Dickstein, Eric Weiss, Niru Maheswaranathan, and Surya Ganguli. Deep unsupervised learning using nonequilibrium thermodynamics. In *International Conference on Machine Learning*, pages 2256–2265. PMLR, 2015.
- Yang Song, Jascha Sohl-Dickstein, Diederik P Kingma, Abhishek Kumar, Stefano Ermon, and Ben Poole. Score-based generative modeling through stochastic differential equations. In *International Conference on Learning Representations*, 2021.
- Yang Song, Prafulla Dhariwal, Mark Chen, and Ilya Sutskever. Consistency models. In *ICML 2023 poster*, 2023.
- Fu-Yun Wang, Zhaoyang Huang, Alexander Bergman, Dazhong Shen, Peng Gao, Michael Lingelbach, Keqiang Sun, Weikang Bian, Guanglu Song, Yu Liu, et al. Phased consistency models. *Advances in neural information processing systems*, 37:83951–84009, 2024.

A Preliminaries

A.1 Itô–Stratonovich Integral Conversion

Let X_t be a semimartingale and $f(t, X_t)$ a sufficiently smooth (e.g., $C^{1,2}$) function. Then the Itô and Stratonovich stochastic integrals are related by the following conversion formula:

$$\int_0^T Y_{t-} \circ dX_t = \int_0^T Y_{t-} \cdot dX_t + \frac{1}{2}[Y, X]_t^c,$$

where \circ denotes the Stratonovich integral and \cdot denotes the Itô integral and $[X, Y]_t^c$ is the continuous part of the covariation.

Example 7. Let $\sigma : \mathbb{R}^+ \rightarrow \mathbb{R}$ and $dX_t = \mu(t, X_t)dt + \sigma_t \circ dW_t$. Then $[\sigma_t, W_t]_t^c = 0$ and hence

$$dX_t = \mu(t, X_t)dt + \sigma_t \circ dW_t = \mu(t, X_t)dt + \sigma_t \cdot dW_t,$$

where μ is sufficiently smooth.

A.2 Stochastic Taylor Approximation

Let $E = \mathbb{R}^d$ and consider the probability space $(C_0^0([0, T], E), \mathcal{F}, \mathbb{P})$, where $\Omega := C_0^0([0, T], E)$ is the space of E -valued continuous functions defined in $[0, T]$ starting at 0 (i.e., the Wiener space), \mathcal{F} is the Borel σ -field and \mathbb{P} is the Wiener measure. By convention, we assume that a path $\omega \in C_0^0([0, T], E)$ is time-augmented, i.e., $\omega^0(t) = t$. We define the coordinate mapping process $W_t^i(\omega) = \omega^i(t), \forall t \in [0, T], i = 1, \dots, d, \omega \in \Omega$. Then under the Wiener measure, $W = (W_t^1, \dots, W_t^d)_{t \in [0, T]}$ is a d -dimensional Brownian motion starting at zeros. Moreover, $\bar{W} = (W_t^0, W_t)_{t \in [0, T]}$ denotes the time-augmented Brownian motion, where $W_t^0 = t$.

We refer readers to Kloeden et al. [1992] and [Milstein, 2013] for a comprehensive treatment of stochastic Taylor expansions for general SDEs. In this section, we focus on the SDE of Eqn. (13), as the backward process of a general diffusion model belongs to this class of SDEs, where the volatility term σ is a scalar function of time t only.

Let $Y := (Y_t)_{t \in [0, T]}$ denote the solution to the following Stratonovich SDE

$$dY_t = \mu(t, Y_t)dt + \sigma_t \circ dW_t, \quad Y_0 = y \in E, \quad (13)$$

where $\mu \in \mathcal{C}([0, T] \times E, E)$ and $\sigma \in \mathcal{C}([0, T], \mathbb{R})$. The solution could be interpreted in the pathwise sense using rough path theory [Lyons and Victoir, 2004].

We next explain the intuition behind the stochastic Taylor approximation. By integrating both sides of Eqn. (13) from s to t , it holds that

$$\begin{aligned} Y_t - Y_s &= \int_s^t \underbrace{\mu(t_1, Y_{t_1})}_{\mu(s, Y_s) + \int_s^{t_1} \partial_t \mu(t_2, Y_{t_2}) dt_2 + \int_s^{t_1} \partial_y \mu(t_2, Y_{t_2}) dY_{t_2}} dt_1 + \int_s^t \underbrace{\sigma_{t_1}}_{\sigma_s + \int_s^{t_1} \partial_t \sigma_{t_2} dt_2} \circ dW_{t_1} \\ &= \int_s^t \mu(s, Y_s) dt_1 + \int_s^t \sigma_s dW_{t_1} + \int_s^t \int_s^{t_1} \partial_t \sigma_{t_2} dt_2 dW_{t_1} + \int_s^t \int_s^{t_1} \partial_y \mu(t_2, Y_{t_2}) \sigma_{t_2} dW_{t_2} dt_1 \\ &\quad + \int_s^t \int_s^{t_1} \partial_y \mu(t_2, Y_{t_2}) \mu(t_2, Y_{t_2}) dt_2 dt_1 + \int_s^t \int_s^{t_1} \partial_t \mu(t_2, Y_{t_2}) dt_2 dt_1. \end{aligned}$$

Note that σ is a function only depending on t and derivatives of σ with respect to y vanish.

Assume that μ has bounded derivatives of all orders and σ has bounded derivatives of at least order 3. Then Y admits the following stochastic Taylor expansion:

$$\begin{aligned} Y_t &= Y_s + \mu(s, Y_s)(t - s) + \sigma_s(W_t - W_s) + \partial_t \sigma_s \int_s^t \int_s^{t_1} dt_2 dW_{t_1} \\ &\quad + \partial_y \mu(s, Y_s) \sigma_s \int_s^t \int_s^{t_1} dW_{t_2} dt_1 + R(t - s). \end{aligned} \quad (14)$$

Note that by integration by parts, $\int_s^t \int_s^{t_1} dt_2 dW_{t_1}$ can be rewritten as

$$\int_s^t (t_1 - s) dW_{t_1} = (t_1 - s)W_{t_1} \Big|_{t_1=s}^t - \int_s^t W_{t_1} dt_1 = (t - s)W_t - \int_s^t W_{t_1} dt_1 \quad (15)$$

$$= (t - s)(W_t - W_s) - \int_s^t (W_{t_1} - W_s) dt_1. \quad (16)$$

Therefore, the dominant term in Eqn. (14) is a function of Y_s , s , and $PS(W)_{s,t}$, where $PS(W)_{s,t} = (t - s, W_t - W_s, \int_s^t (W_{t_1} - W_s) dt_1)$. Therefore, this yields the local expansion:

$$Y_t - Y_s = F(s, Y_s, PS(W_{s,t})) + R(t - s), \quad (17)$$

where the function $F : \mathbb{R}^+ \times E \times \mathbb{R}^+ \times E \times E \rightarrow E$ is defined as

$$F(s, y, s_1, s_2, s_{21}) = \mu(s, y)s_1 + \sigma_s s_2 + \partial_t \sigma_s (s_1 s_2 - s_{21}) + \partial_y \mu(s, y) \sigma_s s_{21}. \quad (18)$$

The remainder term $R(t - s) \equiv Y_t - Y_s - F(s, Y_s, PS(W_{s,t}))$ has a (local) error of strong order $\mathcal{O}((t - s)^2)$.

Numerical approximation of SDEs. For simplicity, consider the equally spaced time partition $D_c := \{t_0, \dots, t_{N_c}\}$ of the time interval $[0, T]$, where $\Delta_c = \frac{T}{N_c}$ and $t_j = j \cdot \Delta_c$ for $j \in \{1, \dots, N_c\}$. Recall that we adopt a higher-order numerical scheme to approximate the solution Y_T as follows. First set $\hat{Y}_{t_0} = Y_0$ and for $i \in \{0, \dots, n_c - 1\}$, set

$$\hat{Y}_{t_{i+1}} = \hat{Y}_{t_i} + F(t_i, Y_{t_i}, PS(W)_{t_i, t_{i+1}}), \quad (19)$$

We use \hat{Y}_T to approximate the solution Y_T to the SDE of Eqn. (13).

Theorem 8 (Numerical approximation theorem). *Assume that μ has bounded derivatives of all orders and σ has bounded derivatives of at least order 3. Let Y and \hat{Y} be defined as before. It holds that*

$$\mathbb{E}[|\hat{Y}_T - Y_T|] \leq C \Delta_c, \quad (20)$$

where C is a constant only depending on μ, σ .

Proof. It is a direct result of the strong error estimate from Kloeden et al. [1992]. \square

A.3 The Signature of a Path

In this subsection, we introduce the definition of path signatures, with a focus on the Stratonovich signature of Brownian motion. We present key properties that are directly relevant to our proposed method. For a comprehensive treatment of path signatures and their desirable mathematical properties as principled and efficient feature representations for time series, we refer readers to Lyons [2014], Levin et al. [2013], Lyons and McLeod [2025].

A.3.1 Path Space

Let $E = \mathbb{R}^d$, equipped with its canonical basis $\{e_1, \dots, e_d\}$. Consider a continuous path $X : J \rightarrow E$, where J is a compact time interval. We introduce the p -variation of the path, which is a commonly used measure to quantify the smoothness of the path.

Definition 9 (p -variation). *Let $p \geq 1$ be a real number. Let $X : J \rightarrow E$ be a continuous path. The p -variation of X on the interval J is defined by*

$$\|X\|_{p,J} = \left[\sup_{D \subset J} \sum_{j=0}^{r-1} |X_{t_{j+1}} - X_{t_j}|^p \right]^{\frac{1}{p}}, \quad (21)$$

where the supremum is taken over any time partition of J , i.e. $D = (t_1, t_2, \dots, t_r)$.

Let $\Omega_p([0, T], \mathbb{R}^d)$ denote the space of continuous d -dimensional paths of finite p -variation starting from the origin. We endow $\Omega_0([0, T], \mathbb{R}^d)$ with the p -variation metric. For each $p \geq 1$, the p -variation norm of a path $X \in \mathcal{C}_p(J, E)$ is denoted by $\|X\|_{p-var}$ and defined as follows:

$$\|X\|_{p-var} = \|X\|_{p,J} + \sup_{t \in J} \|X_t\|.$$

A.3.2 Tensor Algebra Space and the Signature

We then introduce the tensor algebra space of $E = \mathbb{R}^d$, where the signature of an E -valued path takes values. Consider the successive tensor powers $E^{\otimes n}$ of E . If one regard the elements e_i as letters, then $E^{\otimes n}$ is spanned by words of length n in the letters $\{e_1, \dots, e_d\}$, and can be identified with the space of real homogeneous non-commuting polynomials of degree n in d variables, i.e., $(e_I := e_{i_1} \otimes \dots \otimes e_{i_n})_{I=(i_1, \dots, i_n) \in \{1, \dots, d\}^n}$. We give the formal definition of the tensor algebra series as follows.

Definition 10 (Tensor algebra space of E). *The space of all formal E -tensors series, denoted by $T((E))$ is defined to be the following space of infinite series:*

$$T((E)) = \left\{ \mathbf{a} = (a_0, a_1, \dots) \mid a_n \in E^{\otimes n}, \forall n \geq 0 \right\}.$$

It is equipped with two operations, an addition and a product defined as follows:

$\forall \mathbf{a} = (a_0, a_1, \dots), \mathbf{b} = (b_0, b_1, \dots) \in T((E))$, it holds that

$$\begin{aligned} \mathbf{a} + \mathbf{b} &= (a_0 + b_0, a_1 + b_1, \dots); \\ \mathbf{a} \otimes \mathbf{b} &= (c_0, c_1, \dots), \end{aligned}$$

where $c_n = \sum_{j=0}^n a_j \otimes b_{n-j}$.

Let $\pi^I : T((E)) \rightarrow \mathbb{R}$ denote a projection map such that

$$a = \sum_{n=0}^{\infty} \sum_{|J|=n} a_J e_{j_1} \otimes \dots \otimes e_{j_n} \mapsto a_I.$$

Definition 11 (The Signature of a path). *Let $X \in \Omega_p([0, T], \mathbb{R}^d)$ for some $p \geq 1$. Then the signature of the path is defined as $(1, \mathbf{X}_{s,t}^1, \dots, \mathbf{X}_{s,t}^n, \dots)$, where*

$$\mathbf{X}_{s,t}^n := \int_{0 \leq t_1 \leq t_2 \leq \dots \leq t_n \leq t} dX_{t_1} \otimes dX_{t_2} \otimes \dots \otimes dX_{t_n} \in E^{\otimes n}.$$

Remark 12. *The signature of the path X can be also written as*

$$S(X) = \sum_{n=0}^{\infty} S^{(i_1, i_2, \dots, i_k)}(X) (e_{i_1} \otimes e_{i_2} \otimes \dots \otimes e_{i_k}), \quad (22)$$

where $S^{(i_1, i_2, \dots, i_k)}(X)$ denotes the iterated integral of x indexed by I , and is defined as

$$S^{(i_1, i_2, \dots, i_k)}(X) = \int_{0 < t_1 < t_2 < \dots < t_k < T} dX_{t_1}^{(i_1)} dX_{t_2}^{(i_2)} \dots dX_{t_k}^{(i_k)}.$$

Example 13 (Signature of a Brownian motion). *Since Brownian motion has finite p -variation for any $p > 2$, there are multiple ways to define its iterated integrals, such as the Itô and Stratonovich integrals Lyons et al. [2007]. Throughout this paper, we adopt the Stratonovich signature of Brownian motion, as it provides the natural basis for solving Stratonovich differential equations driven by Brownian paths.*

The precise definition of the p -geometric rough path can be found in Lyons et al. [2007]. Roughly speaking, a p -geometric rough path is a generalization of the signature of a path. It is defined via the limit of the signature of bounded 1-variation paths under the p -variation metric for some $p \geq 1$. Notably, the Stratonovich signature is a geometric p -rough path.

Remark 14 (Connection between partial signature and signature). *Let \bar{W} denote the time-argmented Brownian motion. Then the signature of $\bar{W}_{[0,t]}$ of degree 2 is given as follows:*

$$(1, \bar{\mathbf{W}}_{[0,t]}^1, \bar{\mathbf{W}}_{[0,t]}^2),$$

where $\bar{\mathbf{W}}_{[0,t]}^1 = (t, W_t)$ and $\bar{\mathbf{W}}_{[0,t]}^2 = \left(\frac{t^2}{2}, \int_0^t s dW_s, \int_0^t W_s ds, \frac{W_t^2}{2} \right)$. It is easy to see that the partial signature of $\bar{W}_{[0,t]}$ is a subset of the signature of $\bar{W}_{[0,t]}$ of degree 2.

Definition 15 (Shuffle product). Let $I := (i_1, \dots, i_k)$ and $J := (j_1, \dots, j_m)$ denote two multi-indices, where $k, m \in \mathbb{N}$ and $i_1, \dots, i_k, j_1, \dots, j_m \in [d]$. Define a multi-index R by

$$R := (r_1, \dots, r_{k+m}) = (i_1, \dots, i_k, j_1, \dots, j_m).$$

The shuffle product of I and J is a finite set

$$I \sqcup J = \{(r_{\sigma(1)}, \dots, r_{\sigma(k+m)}) | \sigma \in (k, m)\text{-shuffle}\},$$

where a permutation σ of the set $[k+m]$ is called a (k, m) -shuffle if $\sigma(1) < \dots < \sigma(k)$ and $\sigma(k+1) < \dots < \sigma(k+m)$.

Lemma 16 (Shuffle product property). Let $S(X)$ denote the geometric rough path. Then for any index I and J , it holds that

$$\pi^I(S(X)) \cdot \pi^J(S(X)) = \pi^{I \sqcup J}(S(X)).$$

Given $S(\bar{W})$ is a geometric rough path where the stochastic integral is understood in the Stratonovich sense, we have that

$$\underbrace{\pi^{(1,2)} S(\bar{W})}_{\int_0^t s dW_s} + \underbrace{\pi^{(2,1)} S(\bar{W})}_{\int_0^t W_s ds} = \underbrace{\pi^{(1)} S(\bar{W}) \cdot \pi^{(2)} S(\bar{W})}_{=tW_t}. \quad (23)$$

Eqn. (23) is essential for our proposed method. Note that the Stratonovich signature of Brownian motion satisfies the shuffle product property, whereas the Itô signature does not.

A.4 Proof of Lemma 4

The proof of Lemma 4 is given as follows.

Proof. Due to the translation invariance of Brownian motion, it is sufficient to prove that W_t and

$$M_t := \int_0^t \int_0^u dW_{s_1} du \text{ have the covariance matrix } \Sigma = \begin{bmatrix} t & \frac{t^2}{2} \\ \frac{t^2}{2} & \frac{t^3}{3} \end{bmatrix}.$$

It is trivial to prove that W_t and M_t have zero mean. As the variance of W_t is t , we only need to compute (1) the variance of M_t and (2) the covariance between W_t and M_t .

(1) Expanding $\int_0^t \int_0^u dW_{s_1} du$ as $\int_0^t W_u du$, it holds that

$$\text{Var} \left(\int_0^t W_u du \right) = \mathbb{E} \left(\int_0^t W_u du \right)^2,$$

as $\int W_u du$ has zero expectation. By direct calculation, we have

$$\begin{aligned} \mathbb{E} \left(\int_0^t \int_0^t W_{u_1} W_{u_2} du_1 du_2 \right) &= \int_0^t \int_0^t \mathbb{E}(W_{u_1} W_{u_2}) du_1 du_2 \\ &= \int_0^t \int_0^t \min(u_1, u_2) du_1 du_2 = \frac{t^3}{3}. \end{aligned}$$

(2) Expanding the covariance between W_t and M_t , we have

$$\text{Cov}(W_t, M_t) = \mathbb{E}[W_t M_t] = \mathbb{E} \left[\int_0^t W_u W_t du \right] = \int_0^t \min(u, t) du = \frac{t^2}{2}.$$

Hence, the variance and covariance are computed as required. \square

B Universality of Sig-DEG model

We state the rigorous version of Theorem 6 as follows.

Theorem 17 (Universality of Sig-DEG). *Let p_{noise} denote a multivariate Gaussian distribution. Suppose that Y denotes the solution to the backward SDE of Eqn. (4) with the vector field (μ, σ) and the terminal condition $Y_T \sim p_{\text{noise}}$. Assume that $(\mu, \sigma) \in \tilde{C}_b^\infty$, which means that μ and σ are infinitely differentiable with all derivatives bounded. Furthermore, assume that μ, σ are $\text{Lip}(\gamma)$ for $\gamma > 2$.*

Fix any compact set $\mathcal{K} \subset S(\Omega_p([0, T], \mathbb{R}^d))$ for $p \in (2, 3)$. For every $\varepsilon > 0$, there exists sufficiently large $N_c > 0$ and N_θ (the neural network used in the recurrence of $G_\theta^{N_c}$), such that

$$\sup_{W \in \mathcal{K}} \|G_\theta^{N_c}(Y_T, T; W) - Y_0\| \leq \varepsilon. \quad (24)$$

Our proof follows the main steps of proving the universality for the Logsig-RNN model [Liao et al., 2019], with adaptations tailored to our statement. This proof requires the pathwise error estimates of the solution, which is provided by rough path theory [Friz and Victoir, 2010].

Proof. Let \hat{Y} denote the estimator of the solution to the SDE using the numerical approximation scheme. By the triangle inequality, it holds that

$$\|G_\theta^{N_c}(Y_T, T; W) - Y_0\| \leq \underbrace{\|G_\theta^{N_c}(Y_T, T; W) - \hat{Y}_0\|}_{E_1} + \underbrace{\|\hat{Y}_0 - Y_0\|}_{E_2}. \quad (25)$$

Note that \mathbf{W} is a p -geometric rough path and (μ, σ) is a $\text{Lip}(\gamma)$ vector field with $\gamma > p$. By Friz and Victoir [2010], there exists a constant $C = C(p, \gamma)$ such that

$$\|Y_T - \hat{Y}_T\| \leq C \sum_{k=1}^N \|(\mu, \sigma)\|_{\text{Lip}(\gamma)}^{\lfloor \gamma \rfloor + 1} \cdot \|\bar{\mathbf{W}}\|_{p\text{-var}; [t_{k-1}, t_k]}^{\lfloor \gamma \rfloor + 1}. \quad (26)$$

It implies that the global error term has the order $(t - s)^{\frac{\lfloor \gamma \rfloor + 1}{p} - 1}$. Therefore, there exists a sufficiently large $N_1 > 0$ such that $E_2 < \frac{\varepsilon}{2}$.

Moreover, by Lemma C.2 in Liao et al. [2019], it holds that there exists sufficiently large $N_2 > 0$ such that

$$E_1 \leq C \|F - N_\theta\|_\infty,$$

where C is a constant. As the fully connected neural network N_θ has the universality property, there exists a neural network N_θ , such that $E_1 \leq \frac{\varepsilon}{2}$. Let $N_c := \max_{i=1,2} N_i$, the desired error bound (Eqn. (24)) is then achieved. \square

C Implementation and Computational Details

C.1 General notes

Code Availability. The complete source code, including model implementations, training scripts, and evaluation tools, will be released publicly to facilitate reproducibility and further research.

Software Environment. All numerical experiments were conducted using Python 3.10.12 and PyTorch 2.5.1 with CUDA 12.4 and cuDNN 9.1 for GPU-accelerated computations. Wasserstein distances between empirical and model-generated distributions in the 1D Gaussian mixture and Rough Bergomi datasets were computed using the POT (Python Optimal Transport) library [Flamary et al., 2021]. For image datasets, generative quality was evaluated using the Fréchet Inception Distance (FID) as implemented in the `pytorch_fid` package.

Hardware Infrastructure. Experiments were executed on two distinct computational platforms:

- **Multi-GPU Workstation.** This system is composed of 5 NVIDIA Quadro RTX 8000 GPUs (each with 49 GB VRAM), although only a single GPU was used per experiment. It runs Ubuntu 22.04.5 LTS and is powered by dual Intel Xeon Gold 6238 CPUs (88 threads in total, 2.10 GHz base frequency), 502 GB RAM, and SSD storage.

- **High-Performance H100 Server.** The 1D distributions and image dataset experiments were performed on a high-performance computing node based on the NVIDIA Grace Hopper architecture. This server features NVIDIA H100 GPUs with 96 GB HBM3 memory and a 72-core Grace CPU.

Optimization. All experiments were optimized using the Adam optimizer [Kingma and Ba, 2015], with learning rates tailored to each specific task. The choice of learning rate was determined via grid search on a validation set.

As network architectures, hyperparameters, and test metrics depend on the dataset, we defer the relevant details to the corresponding subsections for each dataset.

C.2 1D Toy Example

C.2.1 Data and additional visualization

1DN is a synthetic one-dimensional toy dataset generated from a bimodal distribution, specifically a mixture of two Gaussian components. Both Gaussian components have a standard deviation of 0.5 and are centred at -2 and $+2$. We sample 10,000 examples from this Gaussian mixture model, allocating 8,000 for training and 2,000 for test. 100 examples from the training set are selected as the validation set. This dataset has two distinct modes, which is useful for evaluating the performance of generative models and density estimators in a controlled, low-dimensional setting. The left plot of Figure 3 shows examples sampled from this mixture distribution at time $t = 0$. During the forward (diffusion) process, noise is gradually added to these samples, transforming them into a standard normal distribution over 300 steps. Conversely, the right plot of Figure 3 illustrates the backward (denoising) process, where the teacher model generates samples starting from the standard normal distribution and progressively reconstructs the original bimodal mixture.

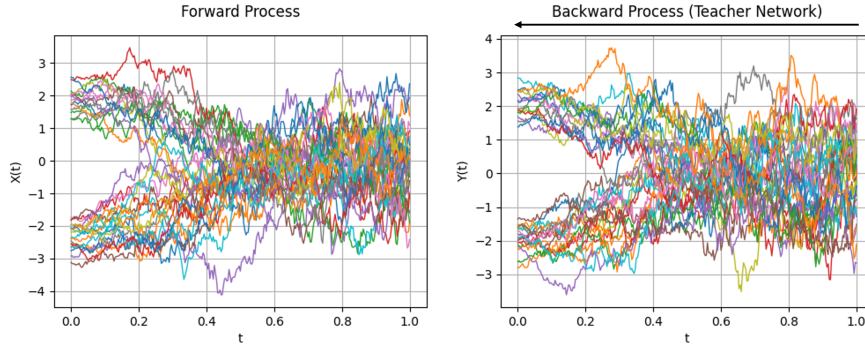


Figure 3: Illustration of the diffusion process on the 1D toy dataset over 300 steps. Left: Samples drawn from the original bimodal mixture of Gaussians at time $t = 0$. Right: Samples generated by the backward (denoising) process of the teacher model, starting from a standard normal distribution and recovering the bimodal structure. The black arrow indicates the direction of the backward process.

C.2.2 Test metrics

For this one-dimensional toy example, we use the following two test metrics to assess the generation quality.

- The Wasserstein-1 distance (denoted by W_1), also referred to as the Earth Mover’s Distance (EMD), was used to quantify the discrepancy between the real and generated one-dimensional distributions.
- The variance score is calculated as the absolute difference between the empirical variances of the real and generated one-dimensional distributions.

C.2.3 Network Details

We define the Residual Architecture, a compact neural network architecture employed in the **IDN** experiment. It combines a residual multi-layer perceptron with explicit time conditioning to facilitate learning over temporally evolving data distributions.

The model takes two inputs:

- A feature vector $x \in \mathbb{R}^{d_x}$, representing the input data.
- A scalar timestep $t \in \mathbb{N}$, used for diffusion-time conditioning.

The model outputs a prediction $\hat{y} \in \mathbb{R}^{d_{out}}$, typically of the same dimensionality as x (i.e., $d_{out} = d_x$).

The forward computation consists of three main stages: temporal embedding, input encoding, and output generation.

Temporal Embedding Module. To incorporate temporal information into the model, a sinusoidal positional encoding is used, yielding an embedding for each discrete time step t , $t_{emb} \in \mathbb{R}^{128}$. This embedding is subsequently processed by a multilayer perceptron defined as follows:

$$\text{MLP}_{\text{time}} := \text{Linear}(128, 256) \rightarrow \text{SiLU} \rightarrow \text{Linear}(256, 256),$$

$$t_{\text{feat}} = \text{MLP}_{\text{time}}(t_{\text{emb}}),$$

where the time-conditioned feature vector $t_{\text{feat}} \in \mathbb{R}^{256}$.

Input Encoding Module. The input vector $x \in \mathbb{R}^{d_x}$ is encoded via a fully-connected residual neural network, denoted $\text{ResNet_FC}(d_x, 256, 3)$. This architecture begins with a linear transformation:

$$\text{Linear}(d_x, 256),$$

and is followed by three residual blocks. Each block consists of two linear layers interleaved with the SiLU activation function and employs a residual connection scaled by $1/\sqrt{2}$ to maintain training stability:

$$h_{i+1} = \frac{1}{\sqrt{2}} (h_i + \text{SiLU}(\text{Linear}(\text{SiLU}(\text{Linear}(h_i))))).$$

This design ensures efficient gradient flow and robust representation learning. The residual network gives an input feature representation $x_{\text{feat}} \in \mathbb{R}^{256}$

$$x_{\text{feat}} = \text{ResNet_FC}(x).$$

Output Module. The encoded representations from the temporal and input modules are combined by element-wise addition, followed by a shallow feedforward neural network to produce the final output:

$$\text{MLP}_{\text{out}} := \text{Linear}(256, 256) \rightarrow \text{SiLU} \rightarrow \text{Linear}(256, d_{\text{out}}),$$

$$y = \text{MLP}_{\text{out}}(x_{\text{feat}} + t_{\text{feat}}).$$

C.3 MNIST data

MNIST [LeCun et al., 1998] is a benchmark dataset of handwritten digits, comprising ten classes representing the digits 0 through 9. It contains 60,000 training images and 10,000 test images, each formatted as a 28×28 grayscale image. During the validation phase, we generate 1,000 images and evaluate their quality by computing the Fréchet Inception Distance (FID) against the training set.

C.3.1 Network Details

Following stable diffusion [Rombach et al., 2022], we first obtain a latent encoding of the image using an auto-encoder and operate the diffusion and denoising process on the latent space. The denoising network used for the teacher model is the same U-Net architecture as described in Rombach et al. [2022]. Specifically, it consists of a symmetric encoder-decoder structure with skip connections, where each level includes multiple ResNet blocks. Self-attention layers are applied at

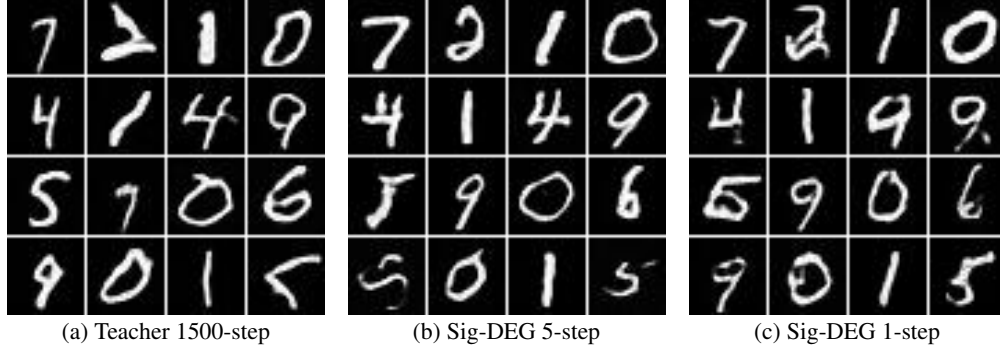


Figure 4: Few-step generation results on the MNIST dataset.

selected resolutions and time embeddings are added to each block to model the diffusion timestep. In the conditional setup, cross-attention layers are also included to enable conditioning on external information such as text embeddings. For our Sig-DEG generator, we introduce an additional input, $PS(W)_{t_i, t_{i-1}}$, which is a Gaussian random variable as described in Lemma 4. To maintain simplicity and computational efficiency, we concatenate this input with the noisy latent encoding along the feature dimension and feed the combined representation into the network. As a result, the primary architectural difference between our Sig-DEG generator and the teacher model lies at the input stage, where the Sig-DEG model incorporates the additional $PS(W)_{t_i, t_{i-1}}$ concatenated with the noisy latent encoding before being passed through the network.

C.3.2 Evaluation Metrics

For image generation tasks, we report the Fréchet Inception Distance (FID) and the Inception Score (IS) as discriminative performance measures. The FID assesses the similarity between the distributions of generated and real image features as extracted by a pre-trained Inception network, while the IS captures the semantic meaningfulness and diversity of generated images.

C.3.3 Hyper-Parameters Choice for Model Complexity Analysis

Full feature dimension: {down channels: [128, 256, 256, 256], mid channels: [256, 256], time embedding: 256}

Three quarter feature dimension: {down channels: [96, 192, 192, 192], mid channels: [192, 192], time embedding: 192}

Half feature dimension: {down channels: [64, 128, 128, 128], mid channels: [128, 128], time embedding: 128}

Between half and one quarter feature dimension: {down channels: [48, 96, 96, 96], mid channels: [96, 96], time embedding: 96}

One quarter feature dimension: {down channels: [32, 64, 64, 64], mid channels: [64, 64], time embedding: 64}

C.3.4 Visual Comparison

We provide the visual comparison for the teacher model (1500 sampling steps) and our proposed Sig-DEG with 5 and 1 sampling steps on the MNIST dataset. As illustrated in Figure 4, even with a single sampling step, our Sig-DEG model is capable of generating clear and recognizable digits, demonstrating the effectiveness of our model.

C.4 Rough Bergomi Task

C.4.1 Data

The rough Bergomi (rBergomi) price process, introduced by Bayer et al. [2016], defines the spot price process as

$$S_t := \exp \left\{ \int_0^t \sqrt{V_u} dB_u - \frac{1}{2} \int_0^t V_u du \right\}, \quad B_u := \rho W_u^1 + \sqrt{1 - \rho^2} W_u^2, \quad (27)$$

$$V_t := \xi \exp \left\{ \eta Y_t^a - \frac{\eta^2}{2} t^{2a+1} \right\}, \quad Y_t^a := \sqrt{2a+1} \int_0^t (t-u)^a dW_u^1, \quad (28)$$

for Brownian motions W^1, W^2 . We sample the process with the help of the hybrid scheme from Bennedsen et al. [2017]. Our dataset is composed of 100 000 sample paths, among which 60% is used for training, 20% for validation, and the remaining 20% is used for testing.

We adopt the standard configuration used in the rough Bergomi dataset, with parameters set as follows: $\xi = 0.235^2$, $\eta = 1.9$, $\rho = -0.9$, $a = -0.35$ (i.e., Hurst parameter of 0.15), $T = 1.0$, and $S_0 = 1.0$.

C.4.2 Test metrics

To evaluate the quality of the generated data, we use several quantitative metrics that assess both marginal distributions and temporal dependencies.

1. **Marginal Distribution Loss.** To evaluate the alignment between the marginal distributions of the generated and reference data, we compute histograms of the marginal probability density functions (PDFs) and measure the average absolute difference between the empirical distributions.
2. **Wasserstein-1 Distance (W_1).** We compute the average W_1 distance between the real and generated time series marginals $X_t^{(i)}$ over all time steps t and feature indices i .
3. **Correlation Discrepancy.** To capture temporal dependencies and cross-feature relationships, we use a correlation-based metric. Let X and \hat{X} denote the real and generated datasets, respectively. The correlation discrepancy is defined as:

$$\text{cor}(X, \hat{X}) = \frac{1}{Td^2} \sum_{s,t} \sum_{i,j=1}^d \left| \rho(X_s^{(i)}, X_t^{(j)}) - \rho(\hat{X}_s^{(i)}, \hat{X}_t^{(j)}) \right|, \quad (29)$$

where $\rho(X, Y)$ denotes the Pearson correlation coefficient between real-valued random variables X and Y . This metric quantifies deviations in both temporal and inter-feature correlation structures.

4. **Autocorrelation Discrepancy.** In order to assess the preservation of temporal dependencies at varying lags, we define an autocorrelation-based loss that compares the lagged autocorrelations of real and generated sequences. Let X and \hat{X} denote the real and generated datasets, respectively, and let $\text{AC}_\tau(\cdot)$ represent the empirical autocorrelation at lag τ . Then, the autocorrelation discrepancy is defined as:

$$\mathcal{L}_{\text{AutoCorr}}(X, \hat{X}) = \frac{1}{L} \sum_{\tau=1}^L \left| \text{AC}_\tau(X) - \text{AC}_\tau(\hat{X}) \right|, \quad (30)$$

where L is the maximum lag considered.

C.4.3 Architecture

We reuse the Residual Architecture from Section C.2.3.

C.4.4 Extended Results

Figure 5 compares pathwise outputs of the **rBerg** teacher and Sig-DEG distilled models across price (top row) and volatility (bottom row). The left panels show the target trajectories in red, the centre panels display teacher-generated samples in green, and the right panels present Sig-DEG outputs in blue. For both price and volatility, the teacher model reproduces the empirical heteroskedasticity and clustered stochastic volatility – key features of financial time series. Sig-DEG closely mirrors these

dynamics despite using significantly fewer sampling steps, only 10 steps are used for Sig-DEG compared with 300 steps for the teacher model.

Figures 6 and 7 display respectively the empirical marginal distributions of standardised log-returns and instantaneous volatilities, over 25 time steps. In both cases, the Sig-DEG model (blue) is compared against the teacher model (green) and the ground-truth distribution (red). The Sig-DEG model, despite relying on only 10 sampling steps, consistently reproduces key statistical features such as the heavy tails of the returns or the skewness. In certain instances, it surpasses the teacher model in reproducing the distribution, demonstrating not only competitive accuracy but also substantial gains in generation speed. Performance of the teacher model deteriorates towards later time steps, likely due to the absence of a memory mechanism such as a recurrent neural network (RNN), which impairs the teacher model’s temporal coherence and, consequently, the quality of the distilled samples from Sig-DEG.

Figures 8 and 9 illustrate the temporal dynamics of the log-return and instantaneous volatility processes, respectively, across six representative dimensions. Each figure presents three sets of trajectories: forward-time samples from the teacher diffusion model (left), backward-time samples from the same teacher model (middle), and intermediate approximations from our model, Sig-DEG (right). The Sig-DEG trajectories are generated using only 10 discretisation steps, yet qualitatively align with the backward samples, indicating the model’s capacity to capture reverse-time dynamics efficiently. Temporal progression is denoted by colour, transitioning from purple to yellow.

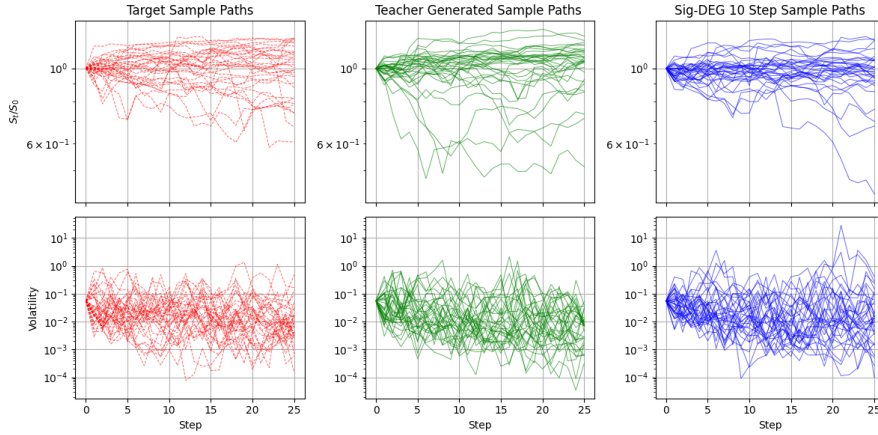


Figure 5: Path samples comparison of Sig-DEG compared to the teacher model and **rBerg** empirical data. The left column shows empirical price and volatility paths in red (target), the centre column contains teacher-generated samples in green, and the right column presents Sig-DEG trajectories in blue (distilled model). All paths are plotted on a logarithmic scale. The teacher model captures key characteristics of financial time series, including expanding price variance and volatility clustering. Sig-DEG effectively replicates these features using only 10 sampling steps, demonstrating robust approximation of high-dimensional diffusion dynamics with minimal temporal resolution.

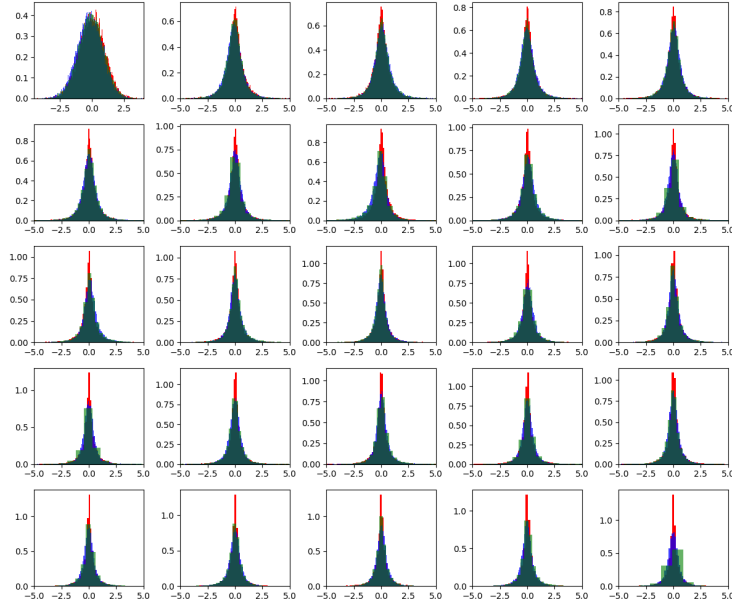


Figure 6: Empirical marginal distributions of standardised log-returns across 25 time steps. Red denotes the ground-truth, green the teacher model, and blue the Sig-DEG model (10 sampling steps). The Sig-DEG model often matches or exceeds the teacher’s performance while achieving significant computational speedup. Degradation in accuracy over time is attributed to the lack of a memory component (e.g., RNN), which limits the teacher’s temporal modelling capacity and, by extension, that of the distilled model.

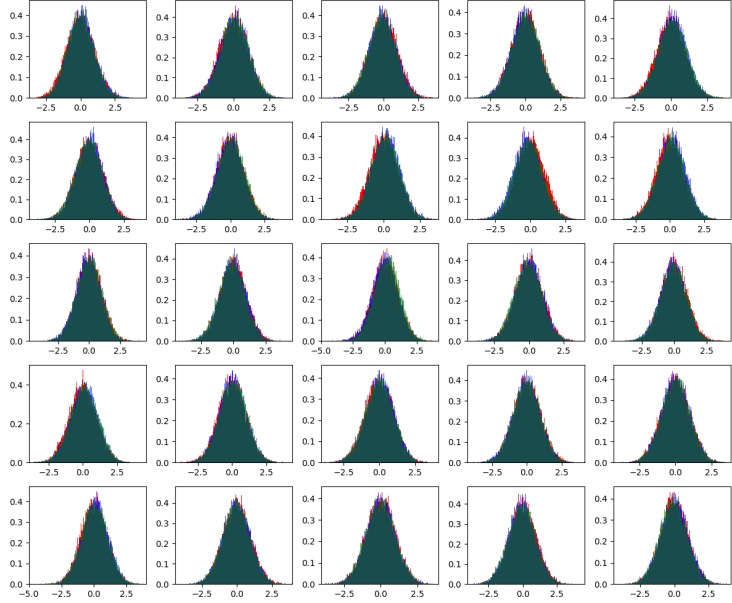


Figure 7: Empirical marginal distributions of standardised log-increments in instantaneous volatility at 25 time steps. The Sig-DEG model (blue) aligns closely with the teacher (green) and ground-truth (red), effectively capturing heavy-tailed and skewed behaviours.

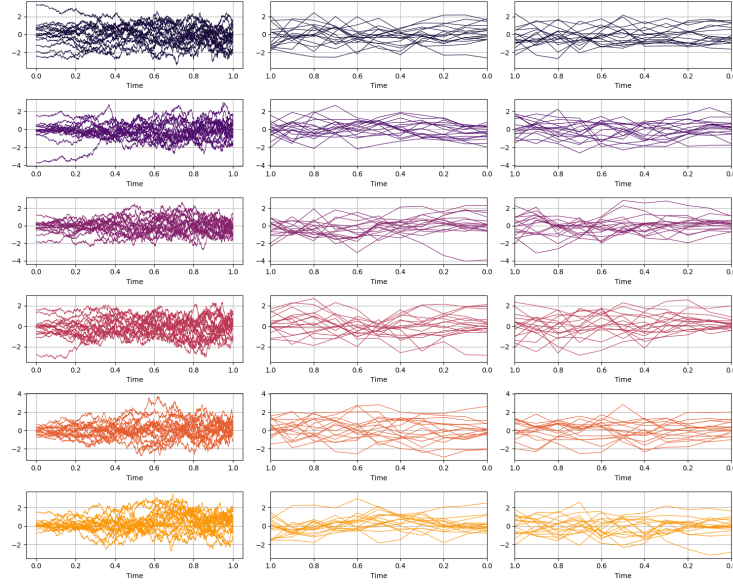


Figure 8: Trajectories of backward process for the log-return process across six representative dimensions. Left: forward-time samples from the teacher diffusion model. Middle: backward-time samples from the teacher diffusion, visualised with the temporal axis reversed. Right: approximate backward-time trajectories generated by Sig-DEG using only 10 discretisation steps. Temporal evolution is encoded via colour, progressing from purple (early) to yellow (late).

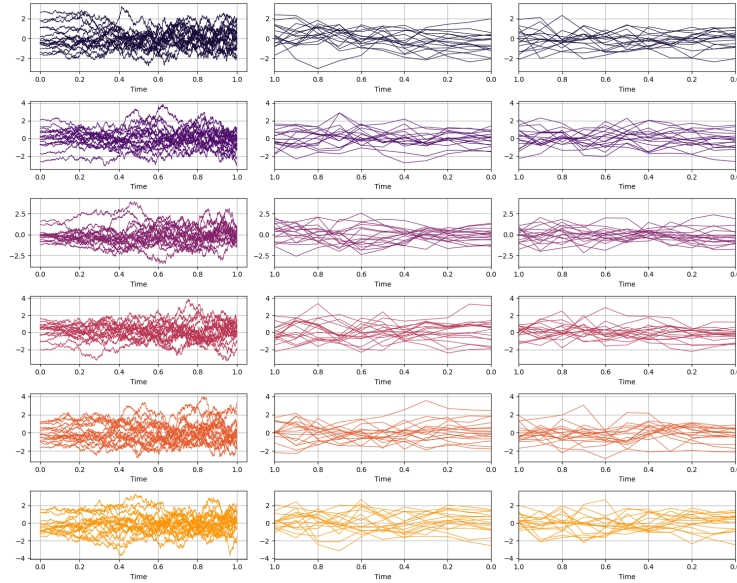


Figure 9: Trajectories of backward process for the instantaneous volatility process across six representative dimensions. Left: forward-time samples from the teacher diffusion model. Middle: backward-time samples from the teacher diffusion, visualised with the temporal axis reversed. Right: approximate backward-time trajectories generated by Sig-DEG using only 10 discretisation steps. Temporal evolution is encoded via colour, progressing from purple (early) to yellow (late).